Received: 18 July 2024 | Revised: 27 August 2024 | Accepted: 16 September 2024

DOI: 10.1002/inf2.12632

RESEARCH ARTICLE

WILEY

Substance discrimination imaging derived from switchable soft and hard x-ray sensing in direct x-ray detector

Jingda Zhao[1] | **Xin Wang**[1] | **Yuwei Li**[1] | **Qi Cheng**[1] | **Damian Chinedu Onwudiwe**[2] | **Byung Seong Bae**[3] | **Mehmet Ertuğrul**[4] | **Ying Zhu**[5] | **Wei Lei**[1] | **Xiaobao Xu**[1]

[1]Joint International Research Laboratory of Information Display and Visualization, School of Electronic Science and Engineering, Southeast University, Nanjing, the People's Republic of China

[2]Department of Chemistry, School of Mathematics and Physical Sciences Faculty of Natural and Agricultural Sciences North-West University, Mafikeng Campus, Mmabatho, South Africa

[3]Department of Electronics & Display Engineering, Hoseo University, Chungnam, Republic of Korea

[4]Faculty of Engineering, Metallurgical and Materials Engineering, Karadeniz Technical University, Trabzon, Turkiye

[5]E-xray Electronic Co. Ltd, Suzhou, the People's Republic of China

Correspondence
Wei Lei and Xiaobao Xu, Joint International Research Laboratory of Information Display and Visualization, School of Electronic Science and Engineering, Southeast University, Nanjing 210096, the People's Republic of China.
Email: xiaobaoxu@seu.edu.cn and lw@seu.edu.cn

Funding information
National Key Research and Development Program of China, Grant/Award Number: 2022YFE0139100; NSFC, Grant/Award Numbers: T2322003, 52172146, 62175028; International Cooperative Research Project of Jiangsu Province, Grant/Award Number: BZ2022008; Fundamental Research Funds for the Central Universities, Grant/Award Number: 2242024K40017

Abstract

Substance discrimination beyond the shape feature is urgently desired for x-ray imaging for enhancing target identification. With two x-ray sources or stacked two detectors, the two-energy-channel x-ray detection can discriminate substance density by normalizing the target thickness. Nevertheless, the artifacts, high radiation dose and difficulty in image alignment due to two sources or two detectors impede their widespread application. In this work, we report a single direct x-ray detector with $MAPbI_3/MAPbBr_3$ heterojunction for switchable soft x-ray (<20 keV) and hard x-ray (>20 keV) detection under one x-ray source. Systematic characterizations confirm soft and hard x-ray deposit their energy in $MAPbI_3$ and $MAPbBr_3$ layer, respectively, while working voltages can control the collection of generated charge carriers in each layer for selective soft/hard x-ray detection. The switching rate between soft and hard x-ray detection mode reaches 100 Hz. Moreover, the detector possesses a moderate performance with ~50 nGy s^{-1} in limit-of-detection, ~8000 μC Gy^{-1} cm^{-2} in sensitivity and ~7 lp/mm in imaging resolution. By defining the attenuation coefficient ratio (μ_I/μ_H) as substance label, we effectively mitigate the influence of target thickness and successfully discriminate substances in the acquired x-ray images.

KEYWORDS

perovskite, photodetector, single crystal, substance discrimination, x-ray imaging

1 | INTRODUCTION

X-ray detection and imaging have been widely used in medical diagnostics, nondestructive testing, security monitoring, and so on.[1–4] Currently, x-ray imaging technologies can be categorized into indirect and direct types. In the indirect method, the scintillator is used to convert x-ray into visible photons, followed by photodiode detection. The direct type utilizes semiconductors directly converting x-ray signal into electrical signal and then read out by an electric field.[5–7] Both the indirect and direct approaches can only produce monochrome images by detecting the x-ray intensity. According to Beer–Lambert's Law, both the substance-related x-ray attenuation coefficient and thickness of the target show a significant influence on x-ray intensity. It is difficult to distinguish their contribution to x-ray intensity variation. Thus, current x-ray images primarily show the shape of targets, with substance information missing, which makes accurate target recognition difficult.

Two-energy-channel x-ray detection can divide the x-ray energy into two channels and can discriminate the difference in object densities by normalizing the thickness influence on intensity variation allowing the enhancement in target identification. To date, two-energy-channel x-ray detection has shown advancements in diagnosing vascular disease, bone mineral density, and so on.[8–10] However, the extreme penetration causes the refractive index of x-ray to be ∼1 in all materials, the optical splitting system or the filter makes no sense for x-ray beam splitting. Thus, current two-energy-channel x-ray detection primarily relies on either two x-ray sources with different anode voltages or two stacked detectors.[8–10] In the former, it significantly increases x-ray radiation and makes it hard to achieve the image alignment, while in the latter, the electrode or circuit on the top detector introduces artifacts in the bottom detector.[11–13] All these make it far from satisfactory in practical application.

Recently, lead halide perovskite materials have emerged as potential candidates for x-ray detectors due to their large $\mu\tau$ product, high absorption coefficient, high photon yield, and low defect density.[14–17] The sensitivity of x-ray perovskite detector has exceeded 10^5 μC Gy^{-1} s^{-1}, and the lowest detection limit is below 100 nGy s^{-1}.[17–19] Additionally, their tunable bandgap and compositional-gradient halide heterojunction with solution epitaxial method[20–23] create the possibilities for designing two-energy-channel x-ray detectors.[24,25] Inspired by the commercial stacked two detectors, the concept of using two different perovskite scintillator layers has been explored in two-energy-channel x-ray detection, in which each scintillator layer converts the x-ray into one color and the multispectral camera captures the scintillating photons.[26] However, the spectral camera significantly increases the overall cost of the system and its small active area requires complicated scanning and a long time to produce images, which harms its practical application. Even worse, high-energy x-ray produce scintillating photons in both scintillator layers, which inevitably leads to the crosstalk in low-energy images. Thus, the facile approach to realize efficient and two-energy-channel x-ray detection is still a challenge.

In this work, we firstly report a direct detector for discriminating soft x-ray (<20 keV) and hard x-ray (>20 keV) by changing working voltage, in which $MAPbI_3/MAPbBr_3$ ($MA = CH_3NH_3$) forming type-I heterojunction is employed as sensing material. The thickness of $MAPbI_3$ layer was set as 60 μm to absorb soft X-rays, while the thickness of $MAPbBr_3$ layer was 1 mm to ensure the absorption of hard x-rays. Systematic characterizations revealed that the alignment of energy levels at heterojunction results in different behaviors of charge carriers under specific electric field conditions. Thus, by adjusting the working voltage, the detector can selectively collect charge carriers from different layers, which results in soft and hard x-ray detection. As a result, our detector exhibits a LOD of 67.6 and 52.1 nGy s^{-1}, sensitivity of 4744.8 and 8169.7 μC Gy^{-1} cm^{-2}, −3 dB with of 2.8 and 15.7 kHz toward sensing soft and hard x-ray, respectively. This device can switch detection between the soft and hard x-ray at a rate of ∼100 Hz. Moreover, by excluding the influence of thickness in the sensing target and using attenuation coefficient ratio as substance label, the detector achieved material discrimination from two-energy-channel x-ray imaging, showcasing its potential practical value.

2 | RESULTS AND DISCUSSION

As we demonstrated above, the strong penetration of x-ray makes filters or optics fail in beam splitting. Consequently, traditional x-ray detectors predominantly operate in energy-integration mode, where the response signal correlates solely with x-ray intensity (I, referring to Figure 1A), allowing only the visualization of target shapes without substance identification. Here, we propose a $MAPbI_3/MAPbBr_3$ heterojunction structure that can regulate carrier dynamics with working voltage, thereby enabling the separate detection of soft and hard x-ray. With substance-related x-ray attenuation coefficient (μ) as contrast in imaging, it holds the promise of achieving target substance imaging with a simple algorithm (Figure 1B).

The $MAPbI_3/MAPbBr_3$ heterojunction was fabricated using the solution epitaxial method, wherein a $MAPbBr_3$

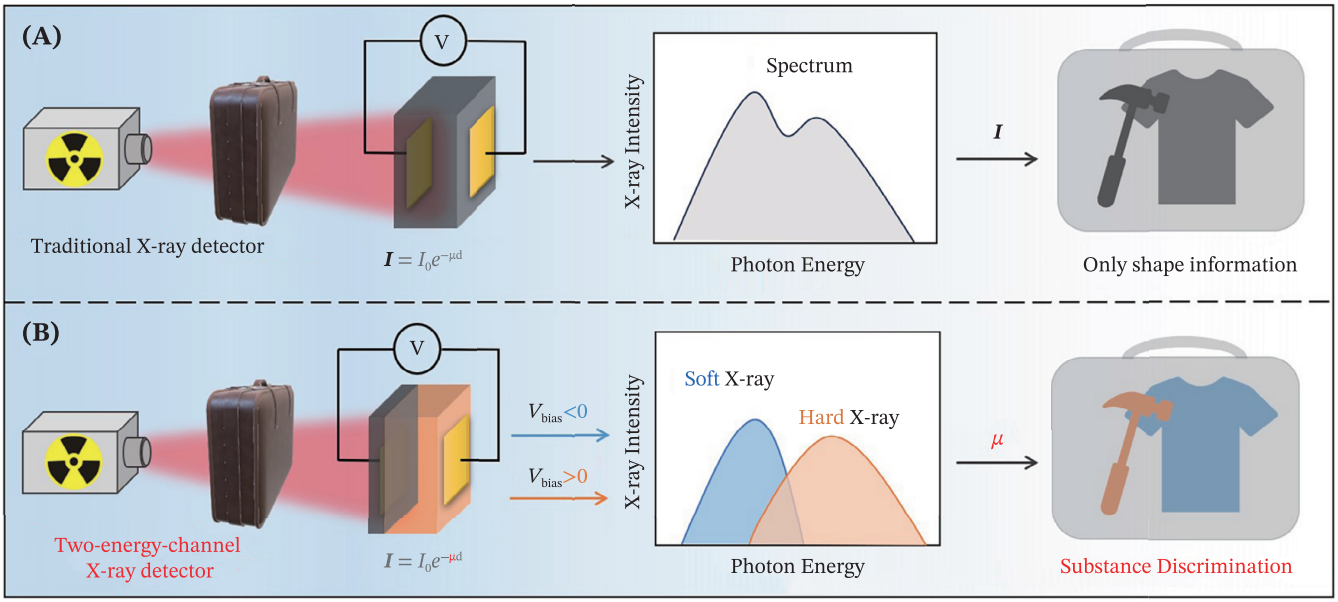

FIGURE 1 Comparison of x-ray images from (A) traditional x-ray detector and (B) our proposed two-energy-channel x-ray detector.

single crystal was immersed into the $MAPbI_3$ precursor solution heated at 100°C (seeing Figure 2A). After 10 min, the $MAPbI_3/MAPbBr_3$ heterojunction was obtained and then polished to a thickness of ~1 mm. Detailed fabrication procedures can be found in the Method section 4.2. Figure 2B shows the photograph of as-fabricated $1 \times 1\ cm^2$ $MAPbI_3/MAPbBr_3$ heterojunction, the bottom $MAPbBr_3$ is translucent, with a smooth surface on the top $MAPbI_3$ side. To control the thickness of epitaxial growth layer, we further investigated the epitaxial growth time of the $MAPbI_3$ layer. Figure S1 shows the top and cross-sectional SEM (scanning electron microscope) images of the $MAPbI_3/MAPbBr_3$ heterojunction with the epitaxial growth time of 2, 5, 10, and 30 min. The epitaxial layer initially grows as the isolated islands and then covers the $MAPbBr_3$ substrate with subsequent vertical growth. Figure 2C presents the cross-section SEM of $MAPbI_3/MAPbBr_3$ heterojunction. No pinholes were observed at the interface. It should be emphasized that the perfect interface is essential to facilitate the carrier transport and suppress the leakage current. Here, the good epitaxial interface can be ascribed to similar lattice constant of $MAPbI_3$ epitaxial layer and $MAPbBr_3$ substrate. Figure 2D displays their x-ray diffraction (XRD) patterns. The sharp characteristic peaks indicate cubic phase in $MAPbBr_3$ substrate and $MAPbI_3$ epitaxial layer, in which the lattice constant was calculated to be 5.938 and 6.110 Å ($f = \frac{a_1 - a_2}{a_1 + a_2}$, where a_1 and a_2 are the lattice constants of the substrate and epitaxial layer), respectively.[21] Thus, the mismatch rate in lattice was estimated as ~1.42%. It is worth noting that the lattice constants of the $MAPbI_3$ epitaxial layer and $MAPbI_3$ single crystal are different, consistent with our previous research.[27,28]

To study the optoelectronic properties of the $MAPbI_3/MAPbBr_3$ interface, we carried out the photoluminescence (PL) measurement under 365 nm excitation. Figure 2E gives the PL spectra. The PL at the interface possesses two distinct peaks that can be assigned to $MAPbBr_3$ and $MAPbI_3$. No additional peak is observed, which implies the absence of halide mixed-phase perovskite like $MAPbBr_xI_{1-x}$ at the interface.[29] Figure S2 presents the energy dispersive x-ray spectroscopy (EDX) revealing the clear change from I to Br elements at the interface. It further confirms a negligible halide ion diffusion at the interface.

Generally, the energy level alignment at the interface plays a crucial influence on charge carrier dynamics, we next studied the band structure of the $MAPbI_3/MAPbBr_3$ heterojunction with the ultraviolet photoelectron spectroscopy (UPS), as shown in Figure 2F. The Fermi level were determined to be −4.91 and −4.86 eV with the valence band maximum of −5.78 and −5.92 eV.[30–32] Since the calculated bandgap of $MAPbI_3$ and $MAPbBr_3$ were 1.62 and 2.13 eV from absorption (Figure 2G), respectively, their conduction band minimum was estimated as −4.16 and −3.79 eV. The type-I heterojunction formed at $MAPbI_3/MAPbBr_3$ interface, as shown in Figure 2H, which allows the unipolar carrier transport under working conditions. Notably, this characteristic is essential for the energy discrimination in our detector since the working voltage can determine the electric field. We will discuss this below.

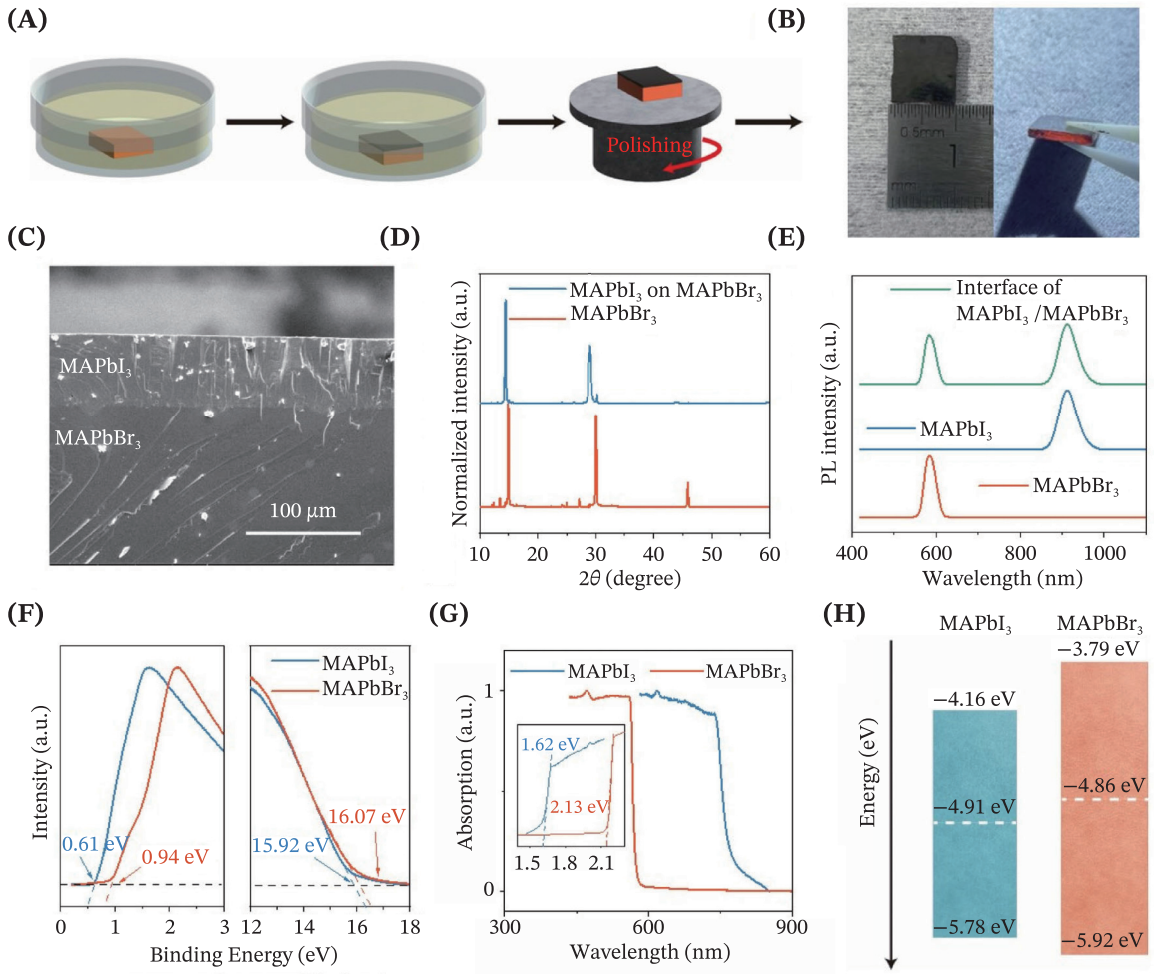

FIGURE 2 Heterojunction fabrication and characterizations. (A) The fabrication process of the $MAPbI_3/MAPbBr_3$ heterojunction. (B) Optical photograph of the $MAPbI_3/MAPbBr_3$ heterojunction with a thickness of ~1 mm. (C) Cross-sectional SEM images of $MAPbI_3/MAPbBr_3$ heterojunction. (D) XRD patterns of $MAPbBr_3$ and $MAPbI_3$ epitaxial layer. (E) PL spectra of $MAPbBr_3$ single crystal, $MAPbI_3$ single crystal, and the interface of $MAPbI_3/MAPbBr_3$ heterojunction. (F) UPS and (G) absorption spectra of $MAPbBr_3$ substrate and $MAPbI_3$ epitaxial layer. (H) The energy band structure of $MAPbBr_3$ substrate and $MAPbI_3$ epitaxial layer.

Figure 3A depicts the schematic diagram of x-ray absorption and the generated charge carriers in $MAPbI_3/MAPbBr_3$ heterojunction. Typically, the penetrating depth of x-rays increases with their energy. Under operation, the $MAPbI_3$ layer faces the x-ray source. Thanks to XCOM, we extract the absorption coefficients of $MAPbI_3$ and $MAPbBr_3$ toward x-rays ranging from 1 to 100 keV, as depicted in Figure 3B. $MAPbI_3$ and $MAPbBr_3$ exhibit a similar value. So, the thickness of the perovskite layer is the predominant factor in controlling the selective absorption of x-ray. Figure 3C shows the calculated penetrating depth of x-ray in the heterojunction, while Figure S3 illustrates their corresponding absorption plots. The result reveals that 60 μm $MAPbI_3$ can absorb almost 100% x-ray with energy less than 10 keV and ~60% at 20 keV. Notably, the sharp fluctuation at 33 keV can be assigned to the K-edge of $MAPbI_3$. Figure S4 presents the calculated generation of electron–hole (e–h) pairs in the heterojunction along its penetrating direction. The distribution of generated carriers can be found in Figure 3D. The e–h pairs generated in the $MAPbI_3$ epitaxial layer mainly originate from soft x-ray absorption, while the $MAPbBr_3$ layer can respond to x-ray photons with energy of greater than 20 keV. The calculation procedure can be found in the Supporting Information.

To reveal the carrier dynamics in detector under work conditions, Figure S5 presents the energy difference at heterojunctions. As the gold electrode contacts with $MAPbI_3$ or $MAPbBr_3$, due to the difference in work functions, a contact potential difference that prevents electrons from entering the electrode, known as a Schottky barrier, is generated. Specify, the energy barriers of 0.19 and 0.24 eV form at the $Au/MAPbI_3$ and $Au/MAPbBr_3$ interfaces, respectively. As $MAPbI_3$ and $MAPbBr_3$ form a

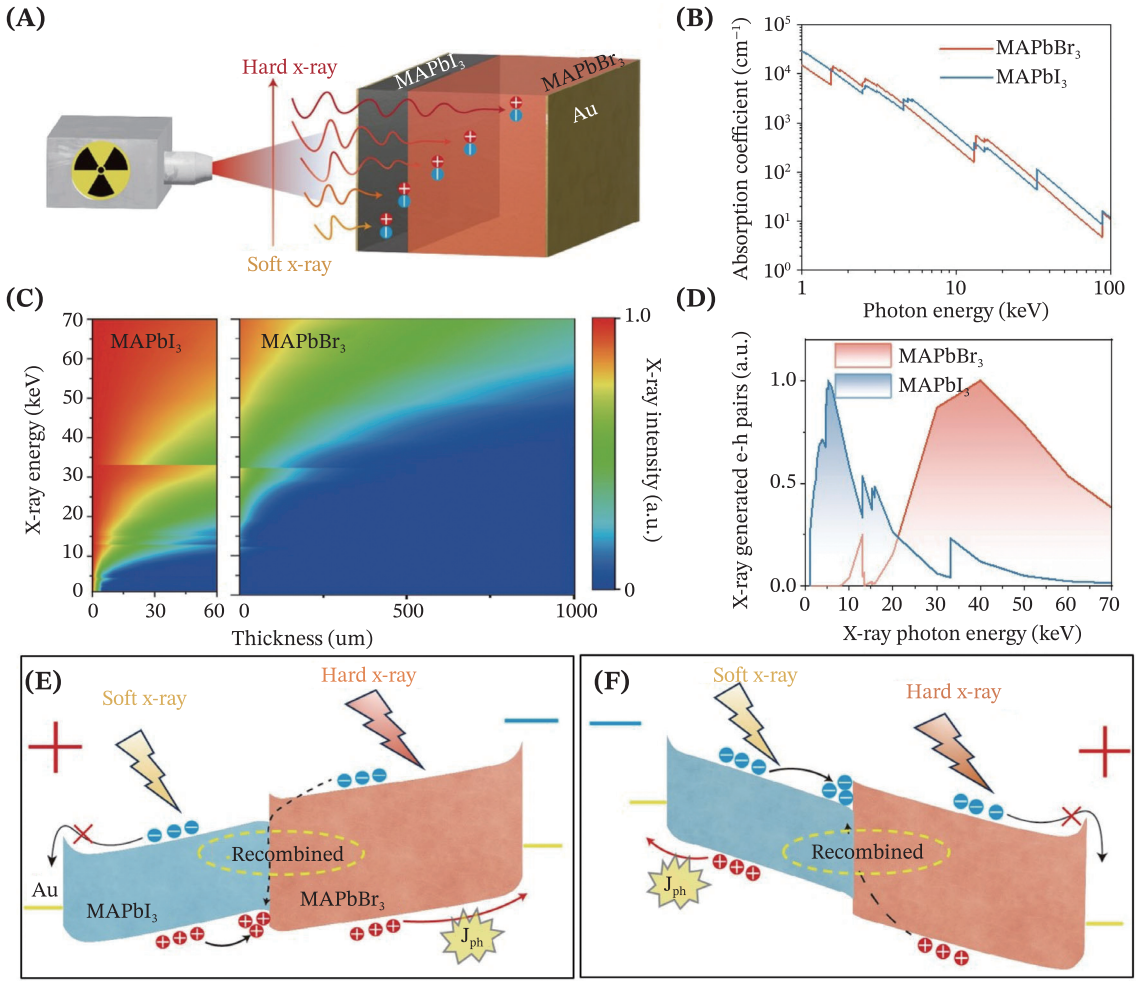

FIGURE 3 The working mechanism for two-energy-channel x-ray detection. (A) Schematic diagram of carrier generation locations when the device is irradiated with x-rays. (B) x-ray absorption coefficients of $MAPbBr_3$ and $MAPbI_3$ with different x-ray photon energies. (C) The normalized intensity of x-rays at different depths within the heterojunction for x-rays of different energies. (D) The x-ray generated electron–hole pairs in the $MAPbI_3$ epitaxial layer and $MAPbBr_3$ substrate exposed under 70 kV X-ray. (E, F) The working principle of our device. In the case of positive bias, only the holes generated by the $MAPbBr_3$ substrate could be collected; only the holes generated by the $MAPbI_3$ epitaxial layer are collected under negative bias.

type-I heterojunction after contact, both electrons and holes struggle to transport from $MAPbI_3$ to $MAPbBr_3$ driven by energy difference ($\Delta E_c = 0.37$ eV and $\Delta E_v = 0.14$ eV). Once $MAPbI_3$ is set as positive bias (forward bias, Figure 3E), the electron generated in $MAPbI_3$ would be blocked at Au/$MAPbI_3$ barrier. At the same time, the hole is accumulated at $MAPbI_3$/$MAPbBr_3$ interface and recombines with electron from $MAPbBr_3$.[33,34] Thus, the hole generated in $MAPbBr_3$ dominates the current in the external circuit, which thereby holds the response toward hard x-ray. When the $MAPbBr_3$ is set as positive bias (reverse bias, Figure 3F), an inverse phenomenon occurs. Electron generated in $MAPbI_3$ is accumulated and recombined at the interface of $MAPbI_3$/$MAPbBr_3$, whereas holes generated in $MAPbI_3$ due to soft x-ray radiation dominate the current.

We separately illuminated the $MAPbI_3$ layer and $MAPbBr_3$ layer using 780 nm red light LED and 530 nm green light LED, respectively. Figure S6 shows that when the $MAPbI_3$ was illuminated, the device responded only under reverse bias. Conversely, when the $MAPbBr_3$ was illuminated with the 530 nm green light, the device responded only under forward bias. These results indicated that the soft x-ray mode detection operates exclusively under reverse bias, while the hard x-ray detection mode operates under forward bias.

Figure 4A illustrates the simulated x-ray energy distribution from various x-ray tube settings using the Spektr 3.0 software. As the x-ray tube voltage increases, the proportion of high-energy x-ray photons gradually rises. Figure 4B presents the current–voltage (I–V) curves in the detector under x-ray radiation, in which the electrode

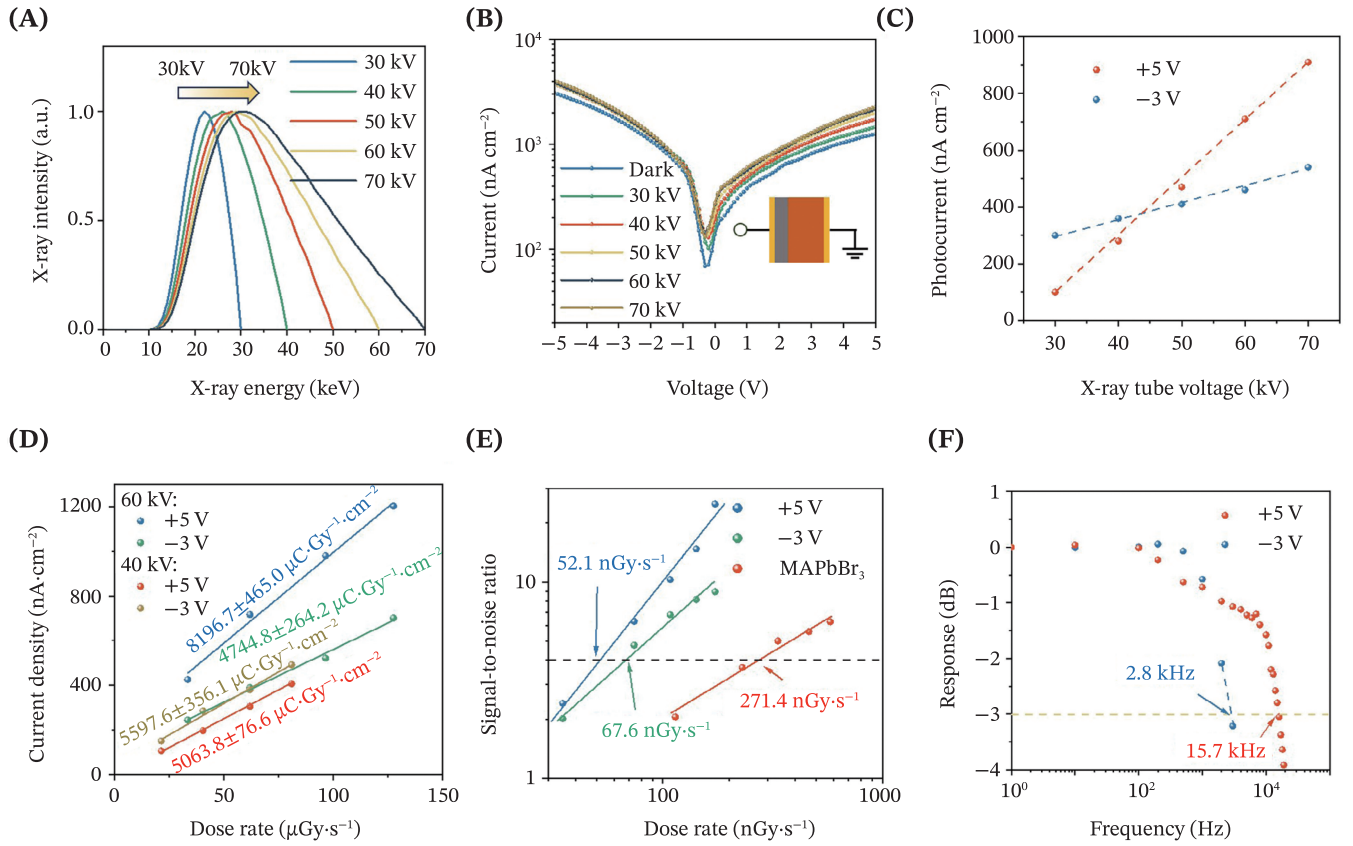

FIGURE 4 Device performance of two-energy-channel x-ray detector. (A) The normalized x-ray energy spectrum of the x-ray source with the tube voltage ranges from 30 to 70 kV. (B) The *I–V* characteristics in dark condition and under irradiation of x-ray with tube voltage range from 30 to 70 kV. (C) The photocurrent in detector versus x-ray with tube voltage range from 30 to 70 kV. (D) The sensitivity of the device operated at 5 and −3 V exposed to the x-ray with a tube voltage of 40 and 60 kV. (E) The LOD of our device operated at 5 and −3 V, and the LOD of 1 mm $MAPbBr_3$ single crystal at 5 V. (F) Temporal response versus the modulated light frequency.

on $MAPbBr_3$ is in contact with the ground. The x-ray tube voltage increased from 30 to 70 kV with the constant tube current. As we can see, the photocurrent density under forward bias shows an obvious change as the x-ray tube voltage varies. This is reasonable because the carriers in $MAPbBr_3$ due to hard x-ray absorption dominate the current. For the negligible variation in current under negative bias, the proportion of low-energy x-ray decreases, but a single high-energy x-ray photon generates more carriers. This result indicates that under positive bias the detector gives the response to the hard x-ray, while it possesses a response to the soft x-ray under negative bias.

Figure 4C presents the extracted current density value versus tube voltage, with 5 and −3 V selected for comparison as their dark current are almost the same. As the tube voltage increases from 30 to 70 kV, the photocurrent density rises from 105 to 912 nA cm^{-2} under 5 V. In contrast, under −3 V bias, the photocurrent density only increases from 293 to 536 nA cm^{-2}. Combined with the results from numerical simulations, it is reasonable to conclude that the working voltage can control the soft and hard x-ray response behavior by regulating the carrier dynamics in the selective layers ($MAPbI_3$ or $MAPbBr_3$).

To comprehensively evaluate device performance, we carried out the characterization on sensitivity, limit-of-detection (LOD), and response width. Figure 4D exhibits the correlation between the photocurrent density and dose rate under x-ray tube voltage of 40 and 60 kV. Under 5 V, the sensitivity of the detector increases from 5063.8 ± 76.6 to 8196.7 ± 465.0 μC Gy^{-1} cm^{-2} as the x-ray tube voltage changes from 40 to 60 kV. As well, under −3 V the sensitivity of the device decreases from 5597.6 ± 356.1 to 4744.8 ± 264.2 μC Gy^{-1} cm^{-2}. This variation can be ascribed to the enhancement in high-energy x-ray photons as x-ray tube voltage increases. For the LOD, our device shows a moderate value of 52.1 and 67.6 nGy s^{-1} under 5 and −3 V bias, respectively (Figure 4E). In comparison, a detector using a 1 mm thick $MAPbBr_3$ single crystal device achieves an LOD of 271.4 nGy s^{-1} at 5 V. The enhancement of LOD in our detector can be attributed to the reduction of noise

current (see Figure S7). The reduction in noise is attributed to the energy barrier's suppression of dark current and the built-in electric field's inhibition of ions migration. Figure S8 shows the Arrhenius plot, the ions activation energy of the heterojunction (434 meV) is greater than that of the $MAPbBr_3$ single crystal (366 meV).[35] This suggests that the heterojunction suppresses ionic migration, consistent with previous reports.[36] More importantly, the baseline of dark current shows negligible change under operation conditions in comparison with that of device based on $MAPbBr_3$ single crystal as sensing material (Figure S9). These results validate that the heterojunction effectively suppresses leakage current, enabling the distinct detection of weak signals.

Furthermore, the temporal response was measured. Herein, we used a green LED in place of x-ray to generate square wave light signals with the assistance of a signal generator. Figure 4F illustrates the dynamic response with the −3 dB cutoff frequency at 15.7 and 2.8 kHz under 5 and −3 V, respectively. This difference arises from the variation in response speed under forward and reverse bias, the device's fall time is 346.4 μs at −3 V bias, significantly slower than that of 194.1 μs at 5 V (see Figure S10). Figure S11 demonstrates stable operation over a period of 500 s at both 5 and −3 V.

As demonstrated above, the primary advantage of our detector lies in its ability to achieve two-energy-channel x-ray detection by adjusting the working voltage. A homemade imaging system was set up to test the material discrimination (Figure 5A). Here, three materials with significantly different densities are chosen as targets: PET (1.3 g cm^{-3}), Al (2.7 g cm^{-3}), and Cu (8.9 g cm^{-3}), each

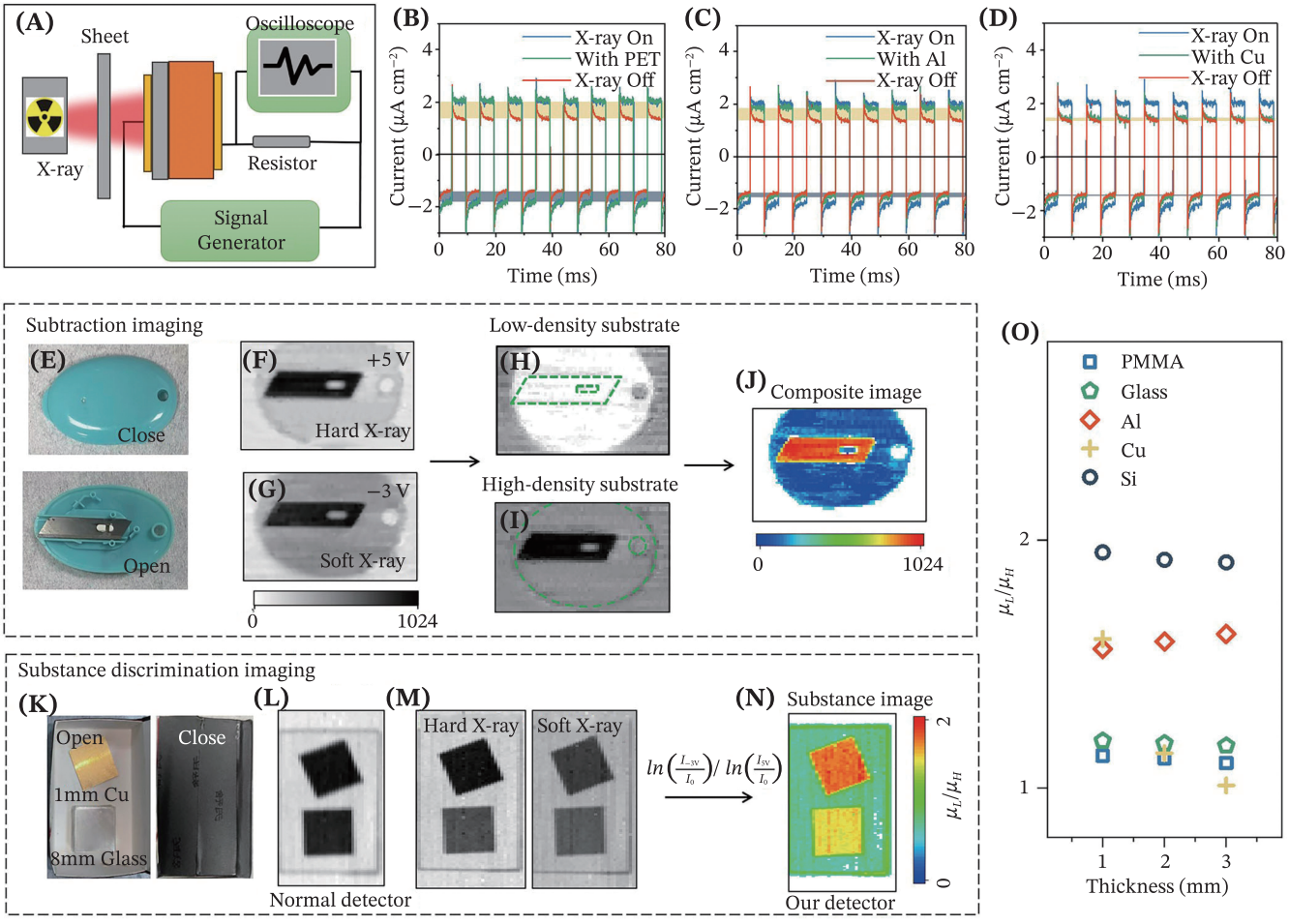

FIGURE 5 Two-energy-channel x-ray imaging and its substance discrimination. (A) The set-up to measure low/hard x-ray signal as a function of time. The current of the device under rapid voltage switching with a (B) PET, (C) Al, and (D) Cu slice positioned between the device and the x-ray tube. The current was recorded by an oscilloscope. (E) Optical image of the paper cutter. The x-ray images captured by our device operated at (F) −3 V and (G) 5 V. The subtraction images of (H) low-density and (I) high-density substrate of the paper cutter. (J) The pseudo-color images. (K) The 1 mm copper sheet and 8 mm glass sheet in a box. The x-ray images of Cu and glass slices obtained by (L) a $MAPbBr_3$ single crystal and images from (M) hard x-ray and soft x-ray. (N) The substance imaging with μ_L/μ_H as a contrast. (O) Substance discrimination in different targets.

with dimensions of 20 × 20 × 1 mm^3. Their x-ray absorption coefficients are illustrated in Figure S12. The device was switched between 5 and −3 V at a frequency of 100 Hz. Figure 5B–D present their response current–time (*I*–*T*) curves toward different targets. For the visual comparison, the dark current and photocurrent without target are also provided. Compared with photocurrent without target, we found that PET causes almost no change in photocurrent under both 5 and −3 V. Al leads to a significant decrease in response current under −3 V, and a slight decrease at 5 V. Cu caused more decrease in photocurrent under 5 V compared to that under −3 V. For soft x-rays, PET exhibits weak absorption, while Al shows higher absorption. Cu possesses a significant stopping power for both soft and hard x-ray. This result gives clear evidence that the working voltage can regulate the distinct response in our detector toward soft and hard x-ray. The results also indicate the potential of our device for discriminating materials.

Digital subtraction imaging has become an important technique in medical diagnosis during the past 10 years. However, it relies on the assistance of contrast agents, for example, the iodine used in digital subtraction angiography. To clarify the potential of our two-energy-channel x-ray detector for digital subtraction imaging, we used the two-energy-channel x-ray detector to image a paper cutter (Figure 5E) at bias voltages of 5 and −3 V. The grayscale differences of the plastic shell are significant due to its different stopping powers toward soft x-rays and hard x-rays (Figure 5F,G). The attenuation of x-rays passing through the two materials follows the formula[37–39]:

$$I = I_0 e^{-\mu_1 d_1 - \mu_2 d_2} \tag{1}$$

in which I is intensity, I_0 is the initial intensity, μ is the attenuation coefficient and d is the thickness, the numbers 1 and 2 represent the plastic and metal components in paper cutter. For overlapping regions, we can modify the x-ray attenuation formula to exclude the influence of objects 1 or 2 as follows:

$$\begin{cases} \ln\left(\frac{I_L}{I_0}\right) = -\mu_{L1} d_1 - \mu_{L2} d_2 \\ \ln\left(\frac{I_H}{I_0}\right) = -\mu_{H1} d_1 - \mu_{H2} d_2 \end{cases} \tag{2}$$

$$\begin{cases} \ln\left(\frac{I_L}{I_0}\right) - \frac{\mu_{L1}}{\mu_{H1}} \ln\left(\frac{I_H}{I_0}\right) = -\left(\mu_{L2} - \frac{\mu_{L1} \cdot \mu_{H2}}{\mu_{H1}}\right) \cdot d_2 \\ \ln\left(\frac{I_L}{I_0}\right) - \frac{\mu_{L2}}{\mu_{H2}} \ln\left(\frac{I_H}{I_0}\right) = -\left(\mu_{L1} - \frac{\mu_{L2} \cdot \mu_{H1}}{\mu_{H2}}\right) \cdot d_1 \end{cases} \tag{3}$$

where L and H indicate the soft and hard x-ray, respectively. As shown in Figure 5H,I, low-density substance and high-density substance in our image are separated through applying the algorithm. The dashed green lines indicate the outline of the substance being subtracted. Further, it allows us to use pseudo-color in different objects in x-ray image, as shown in Figure 5J, in which the blue areas represent low-density objects, and the red areas represent high-density objects. It is worth to noting that subtraction imaging can only distinguish the known objects in images.

Substance discrimination in x-ray images can further enhance the target identification. Taking medical diagnosis as an example, two-energy-channel x-ray detection can exclude the thickness of organic tissues (like blood vessels, fat, muscle, etc) in imaging, allowing doctors to identify them separately and thereby improving diagnostic accuracy. To evaluate our detector in substance imaging, we chose glass sheet and copper sheet in the box as imaging targets and carefully set their thickness to 8 and 1 mm, respectively (Figure 5K). This thickness allows the glass sheet to block most of the hard x-rays. Figure 5L shows the images of glass and copper sheets obtained by a $MAPbBr_3$ single crystals x-ray detector, where their grayscale values are very similar and difficult to distinguish. In real scenarios, this phenomenon is common and it is hard to figure out the targets from x-ray images.

To extract the substance information, we employ a logarithm transformation followed by division to exclude the influence of thickness as follows:

$$\begin{cases} \ln\left(\frac{I_L}{I_{L0}}\right) = -\mu_L d \\ \ln\left(\frac{I_H}{I_{H0}}\right) = -\mu_H d \end{cases} \tag{4}$$

$$\frac{\ln\left(\frac{I_L}{I_{L0}}\right)}{\ln\left(\frac{I_H}{I_{H0}}\right)} = \frac{\mu_L}{\mu_H} \tag{5}$$

We used our detector to capture x-ray images in soft and hard x-ray detection modes separately (Figure 5M). Then we applied the aforementioned algorithm to calculate the μ_L/μ_H ratio (x-ray attenuation coefficient ratio) of the image. As shown in Figure 5N, it can significantly enlarge the difference between glass and copper plates in the images, which ensures us to distinguish the glass and copper plates. Actually, we further explore the application of our two-energy-channel detection for discriminating the targets, the μ_L/μ_H ratio for different substances is shown in Figure 5O. The μ_L/μ_H value in low-density materials (like PMMA, glass, Si, and Al) almost keeps constant as their thickness changes. The result presents the advance of our dual energy detector for recognizing

materials. Notably, the ratio changes significantly for copper with different thicknesses. This is reasonable since the thick copper can almost completely block low-energy x-rays and increase the deviation in μ_L/μ_H. Therefore, for high-density materials, differentiation requires higher-energy x-rays. Moreover, the imaging system shows a high spatial resolution of 7.2 lp mm^{-1} from the modulation transfer function (MTF) (Figure S13).

3 | CONCLUSION

In conclusion, to address the challenges of two-energy-channel x-ray detection and imagining due to two x-ray sources or stacked two detectors, we design and fabricate a single detector for switchable soft and hard x-ray detection under a single x-ray source. With $MAPbI_3$/$MAPbBr_3$ heterojunction as the sensing material, our characterizations reveal that the type-I energy structure at the heterojunction enables the regulation of carrier dynamics in $MAPbI_3$ or $MAPbBr_3$ through the applied working voltage. As a result, by switching the −3 or 5 V working voltage, we achieve selective responses to soft and hard x-ray in a single detector. The switching rate between soft and hard x-ray detection reaches ∼100 Hz. With the assistance of an algorithm, the imaging with our detector demonstrates significant advancement in discriminating different materials. Meanwhile, the detector exhibits a LOD of 52.1 nGy s^{-1}, sensitivity of 8169.7 μC Gy^{-1} cm^{-2}, −3 dB with of 15.7 kHz, which demonstrates the potential of our two-energy-channel device in practical applications.

4 | METHODS

4.1 | Materials

Lead bromide ($PbBr_2$, 99%), lead iodide (PbI_2, 99%), methylammonium bromide (MABr), and methylammonium iodide (MAI) were purchased from Sigma Aldrich, USA. Dimethylformamide (DMF) and γ-Butyrolactone (GBL) were purchased from Aladdin. All products were used as received.

4.2 | Fabricated of the two-energy-channel x-ray detector

Inverse temperature crystallization method was utilized to obtained $MAPbBr_3$ single crystal, 1 mol L^{-1} MABr and $PbBr_2$ was dissolved in 50 mL DMF, then the solution was transferred into a crystallizing dish the temperature raised from 40°C to 60°C at a rate of 0.5°C per hour. 1 mol L^{-1} MAI and PbI_2 was dissolved in 30 mL GBL to obtain the $MAPbI_3$ precursor, the $MAPbBr_3$ single crystal was immersed into $MAPbI_3$ precursor heated at 110°C. After 10 min, the $MAPbI_3$/$MAPbBr_3$ heterojunction was obtained. Then we polished the heterojunction to 1 mm, and the gold electrodes with the thickness of 50 nm were evaporated onto both sides.

4.3 | Characterization

An X'TRA system with a Cu target (Switzerland) was used to obtain x-ray diffraction (XRD) patterns. A Quanta 200 FEI microscope was used to obtain the scanning microscopy (SEM) images. Ultraviolet photoelectron spectroscopy (UPS) was obtained using a PHI 5000 VersaProbe (Japan). The PL was measured using a SpectraMax instrument (UK). The response speed was carried out with an Agilent oscilloscope (7.5 GHz, USA), a signal generator and a Keithley 2400 voltage source (USA). The *I–T*, *I–V* characteristics, and sensitivity were obtained by Keithley 2400 voltage source (USA). The simulated calculation was carried out using MATLAB and COMSOL. X-ray was generated by an Amptek Mini-X2. The x-ray images were obtained by using a *x–y* scanning system to move the object between the detector and x-ray source.

AUTHOR CONTRIBUTIONS

W. L. and X. X. supervise this project. Y. L. grown the single crystal. J. Z. fabricated the device and did the simulated calculation. J. Z. and Q. C. carried out the primal optical, electronic characterizations, and x-ray detection. J. Z. and X. W. prepared the manuscript with revisions from W. L. and X. X. All authors discussed the results and confirmed the manuscript.

ACKNOWLEDGMENTS

This work at SEU was financially supported by National Key Research and Development Program of China (2022YFE0139100), NSFC (Nos. T2322003, 52172146, 62175028), International Cooperative Research Project of Jiangsu Province (BZ2022008), and the Fundamental Research Funds for the Central Universities (No. 2242024K40017).

CONFLICT OF INTEREST STATEMENT

The authors declare no conflict of interest.

ORCID

Xiaobao Xu https://orcid.org/0009-0009-7738-5336

REFERENCES

1. Taguchi K, Iwanczyk JS. Vision 20/20: single photon counting x-ray detectors in medical imaging: vision 20/20: photon counting detectors. *Med Phys*. 2013;40(10):100901.
2. Zhao J, Wang X, Ding Y, et al. A flexible perovskite homojunction with metallic ion doping for large-scale and high sensitivity x-ray detection. *J Mater Chem A*. 2023;11(16):9049-9056.
3. Wu H, Ge Y, Niu G, Tang J. Metal halide perovskites for x-ray detection and imaging. *Matter*. 2021;4(1):144-163.
4. Kakavelakis G, Gedda M, Panagiotopoulos A, Kymakis E, Anthopoulos TD, Petridis K. Metal halide perovskites for high-energy radiation detection. *Adv Sci*. 2020;7(22):2002098.
5. Zhou Y, Chen J, Bakr OM, Mohammed OF. Metal halide perovskites for x-ray imaging scintillators and detectors. *ACS Energy Lett*. 2021;6(2):739-768.
6. Yakunin S, Sytnyk M, Kriegner D, et al. Detection of x-ray photons by solution-processed lead halide perovskites. *Nature Photon*. 2015;9(7):444-449.
7. Kim YC, Kim KH, Son DY, et al. Printable organometallic perovskite enables large-area, low-dose x-ray imaging. *Nature*. 2017;550(7674):87-91.
8. Lorente Ramos RM, Azpeitia Armán J, Arévalo Galeano N, Muñoz Hernández A, García Gómez JM, Gredilla MJ. Dual energy x-ray absorptimetry: fundamentals, methodology, and clinical applications. *Radiología (English Edition)*. 2012;54(5):410-423.
9. Goo HW, Goo JM. Dual-energy CT: new horizon in medical imaging. *Korean J Radiol*. 2017;18(4):555.
10. Rebuffel V, Dinten JM. Dual-energy x-ray imaging: benefits and limits. *Insight - Non-Destructive Testing and Condition Monitoring*. 2007;49(10):589-594.
11. Ran P, Yang L, Jiang T, et al. Multispectral large-panel x-ray imaging enabled by stacked metal halide scintillators. *Adv Mater*. 2022;34(42):2205458.
12. Hu X, Luo S, Leng J, et al. Density-discriminating chromatic x-ray imaging based on metal halide nanocrystal scintillators. *Sci Adv*. 2023;9(37):eadh5081.
13. Pang J, Zhao S, Du X, Wu H, Niu G, Tang J. Vertical matrix perovskite x-ray detector for effective multi-energy discrimination. *Light Sci Appl*. 2022;11(1):105.
14. Shi D, Adinolfi V, Comin R, et al. Low trap-state density and long carrier diffusion in organolead trihalide perovskite single crystals. *Science*. 2015;347(6221):519-522.
15. Dong Q, Fang Y, Shao Y, et al. Electron-hole diffusion lengths >175 μm in solution-grown $CH_3NH_3PbI_3$ single crystals. *Science*. 2015;347(6225):967-970.
16. Saidaminov MI, Abdelhady AL, Murali B, et al. High-quality bulk hybrid perovskite single crystals within minutes by inverse temperature crystallization. *Nat Commun*. 2015;6(1):7586.
17. Zhao L, Zhou Y, Shi Z, et al. High-yield growth of $FACsPbBr_3$ single crystals with low defect density from mixed solvents for gamma-ray spectroscopy. *Nat Photon*. 2023;17(4):315-323.
18. Wei H, DeSantis D, Wei W, et al. Dopant compensation in alloyed $CH_3NH_3PbBr_3{-}xClx$ perovskite single crystals for gamma-ray spectroscopy. *Nat Mater*. 2017;16(8):826-833.
19. Pan W, Wu H, Luo J, et al. $Cs_2AgBiBr_6$ single-crystal x-ray detectors with a low detection limit. *Nat Photonics*. 2017;11(11):726-732.
20. Yang M, Zhang T, Schulz P, et al. Facile fabrication of large-grain $CH_3NH_3PbI_3{-}xBrx$ films for high-efficiency solar cells via CH_3NH_3Br-selective Ostwald ripening. *Nat Commun*. 2016;7(1):12305.
21. Wang X, Li Y, Xu Y, et al. Solution-processed halide perovskite single crystals with intrinsic compositional gradients for x-ray detection. *Chem Mater*. 2020;32(12):4973-4983.
22. Wang X, Xu Y, Pan Y, et al. Low-noise x-ray PIN photodiodes made of perovskite single crystals by solution-processed dopant incorporated epitaxial growth. *Nano Energy*. 2021;89:106311.
23. Saidaminov MI, Haque MA, Savoie M, et al. Perovskite photodetectors operating in both narrowband and broadband regimes. *Adv Mater*. 2016;28(37):8144-8149.
24. Li L, Chen H, Fang Z, et al. An electrically modulated single-color/dual-color imaging photodetector. *Adv Mater*. 2020;32(24):1907257.
25. Kim H, Kim W, Pak Y, et al. Bias-modulated multicolor discrimination enabled by an organic–inorganic hybrid perovskite photodetector with a p-i-n-i-p configuration. *Laser Photonics Rev*. 2020;14(11):2000305.
26. Su Y, Ran P, Hui J, Yang Y. Quantitative dual-energy x-ray imaging based on K-edge absorption difference. *J Phys Chem Lett*. 2023;14(44):10074-10079.
27. Xu Y, Wang X, Zhao J, et al. Solution-processed epitaxial growth of $MAPbI_3$ single-crystal films for highly stable photodetectors. *Front Mater*. 2021;8:651957.
28. Xu Y, Wang X, Pan Y, et al. Perovskite photodetectors based on p-i-n junction with epitaxial electron-blocking layers. *Front Chem*. 2020;8:811.
29. Zhou J, Luo J, Rong X, et al. Lead-free perovskite derivative $Cs_2SnCl_6{-}xBrx$ single crystals for narrowband photodetectors. *Adv Opt Mater*. 2019;7(10):1900139.
30. Chen Q, Chen L, Ye F, et al. Ag-incorporated organic–inorganic perovskite films and planar heterojunction solar cells. *Nano Lett*. 2017;17(5):3231-3237.
31. Song J, Cui Q, Li J, et al. Ultralarge all-inorganic perovskite bulk single crystal for high-performance visible-infrared dual-modal photodetectors. *Adv Opt Mater*. 2017;5(12):1700157.
32. Liang F, Jiang J, Zhao Y, et al. Fabrication of $MAPbBr_3$ single crystal p-n photodiode and n-p-n phototriode for sensitive light detection application. *Adv Funct Mater*. 2020;30(32):2001033.
33. Liu J, Hao Q, Gan H, et al. Selectively modulated photoresponse in type-I heterojunction for ultrasensitive self-powered photodetectors. *Laser Photonics Rev*. 2022;16(11):2200338.
34. Luo Z, Xu H, Gao W, et al. High-performance and polarization-sensitive imaging photodetector based on WS_2/Te tunneling heterostructure. *Small*. 2023;19(15):2207615.
35. Xing J. Ultrafast ion migration in hybrid perovskite polycrystalline thin films under light and suppression in single crystals. *Phys Chem Chem Phys*. 2016;18(44):30484-30490.

36. Zhang X, Chu D, Jia B, et al. Heterointerface design of perovskite single crystals for high-performance x-ray imaging. *Adv Mater*. 2023;36(3):2305513. doi:10.1002/adma.202305513
37. Devanathan R, Corrales LR, Gao F, Weber WJ. Signal variance in gamma-ray detectors—a review. *Nucl Instrum Methods Phys Res, Sect A*. 2006;565(2):637-649.
38. Wei H, Fang Y, Mulligan P, et al. Sensitive x-ray detectors made of methylammonium lead tribromide perovskite single crystals. *Nat Photonics*. 2016;10(5):333-339.
39. Zhao J, Zhao L, Deng Y, et al. Perovskite-filled membranes for flexible and large-area direct-conversion x-ray detector arrays. *Nat Photonics*. 2020;14(10):612-617.

SUPPORTING INFORMATION

Additional supporting information can be found online in the Supporting Information section at the end of this article.

How to cite this article: Zhao J, Wang X, Li Y, et al. Substance discrimination imaging derived from switchable soft and hard x-ray sensing in direct x-ray detector. *InfoMat*. 2025;7(2):e12632. doi:10.1002/inf2.12632